Microelasticity model of random alloys, Part II: Displacement and stress correlations

Pierre-Antoine Geslin, Ali Rida, David Rodney

Microelasticity model of random alloys. Part II: displacement and stress correlations

Pierre-Antoine Geslin

Univ. Lyon, CNRS, INSA Lyon, UCBL, MATEIS, UMR5510, 69621 Villeurbanne, France

E-mail: pierre-antoine.geslin@insa-lyon.fr

Ali Rida

Univ. Lyon, CNRS, INSA Lyon, UCBL, MATEIS, UMR5510, 69621 Villeurbanne, France

E-mail: ali.rida.1993@hotmail.com

David Rodney

Univ. Lyon, Université Claude Bernard Lyon 1, CNRS, Institut Lumière Matière, 69622 Villeurbanne, France

E-mail: david.rodney@univ-lyon1.fr

Abstract. In this two-part article, we propose elastic models of disordered alloys to study the statistical properties of the random displacement and stress fields emerging from the random distributions of atoms of different sizes. In Part I, we presented real- and Fourier-space approaches enabling to obtain the amplitude of the fluctuations through the mean square displacements and stresses. In the present Part II, we extend the Fourier approach to address spatial correlations. We show that, even if the alloy is fully disordered and elastically isotropic, correlations are highly anisotropic. Our continuum predictions are validated by comparisons with atomistic models of random alloys. We also discuss the consequence of displacement correlations on finite size effects in atomistic calculations and on diffuse X-ray and neutron scattering experiments and the possible implications of stress correlations on dislocation behavior.

Random alloys are solid solutions of two or more components where atoms of different nature are located randomly on the crystalline lattice. The plasticity of random alloys has been of significant interest for several decades [1, 2, 3] but has recently attracted a renewed attention with the development of high entropy alloys (HEA) [4, 5, 6]. The size difference between the alloy components induces displacements of the atoms from their lattice sites, as well as internal stresses. These atomic displacements, also referred to as "lattice distortion" in the literature [5, 6] have been the focus of multiple studies because they were found to correlate well with solid solution strengthening and can be assessed by both experimental (using X-ray [5, 7, 8, 9, 10] and

neutron diffraction [11, 12]) and numerical methods [13, 14, 15, 16]. By way of contrast, internal stresses have been much less studied probably partly because they are more difficult to measure in experiments. However, internal shear stresses are of central importance since they induce Peach-Koehler forces that impede dislocation motion and thus control the yield stress and the corresponding solid solution strengthening. Therefore, it appears highly desirable to assess both displacement and stress fields in random alloys in order to better understand the relations between the atomic size differences, atomic displacements and the yield stress of the alloys.

In Part I [17] of this two-part paper, we presented two different elastic models of random alloys where atoms of different sizes are modeled as elastic inclusions embedded in a continuous elastic medium. The real-space model described in Part I combines Nöhring and Curtin's statistical treatment [18] with an elastic model: the displacement (and stress) on an atomic site is obtained as the sum of the contributions of all surrounding atoms that are treated as Eshelby inclusions characterized by dilatational eigenstrains. This approach yields expressions for the mean square displacement and stress as a function of infinite sums over all lattice sites that can be computed numerically. We also proposed a Fourier-based approach that relies on the microelasticity framework [19, 20]. To facilitate calculations in Fourier space, the atomic eigenstrains are spread over a small distance a with a Gaussian distribution around the atomic sites. This approach yields analytical expressions of the mean square displacement and stress that are obtained after averaging everywhere in space. These quantities do not depend on the crystalline structure but are functions of the free parameter a. Both real- and Fourier-based approaches yield similar expressions for the mean square displacement and stress, both proportional to the variance of the eigenstrains in the alloy and differing only by a geometric prefactor. While Part I focuses on the mean-square displacement and stress, the present Part II is dedicated to the spatial correlations of these fields.

The spatial correlations between atomic displacements are of significant importance both for numerical and experimental studies. First, a better understanding of the spatial correlations would help assess the influence of finite system size and boundary conditions on simulation results. Also, atomic displacements are known to affect the intensity obtained in X-ray and neutron scattering experiments. While fluctuations of displacements influence the intensity and broadening of the Bragg peaks [5, 7, 8, 9, 10], correlations induce diffuse scattering and in particular Huang scattering near the Bragg peaks [21, 22, 23]. Also, Glas [24] demonstrated numerically the presence of long-range displacement correlations in an atomistic model of semiconductor and showed how the correlations modify the contrast obtained in transmission electronic microscopy (TEM).

The spatial correlations between shear stresses are central to characterize the stress environment impeding dislocation glide in random alloys. Without correlations, basic scaling arguments [25, 26] can be used to show that, in a line tension model, the yield

stress grows with the variance of the shear stress field with a 2/3 exponent:

$$\tau_{y0} \sim \frac{\langle \tau^2 \rangle^{2/3}}{\Gamma^{1/3}}, \tag{1}$$

where Γ is the dislocation line tension. This scaling is affected by stress correlations [25, 27, 28] that necessarily exist in disordered three-dimensional isotropic solids and exhibit a $1/d^3$ power-law decay at long range, as demonstrated by Lemaître [29, 30, 31]. Assessing the stress correlations appears therefore crucial to better understand dislocation behavior in random alloys. However, we note that, so far, the effect of stress correlations has not been investigated in energy-based [2, 32, 33, 34] or stress-based [26, 35] dislocation models.

The real space approach described in Part I [17] can be used to express spatial correlations. However, the resulting expressions are functions of intertwined infinite sums that are difficult to interpret and analyse. In this Part II, we prefer to extend the Fourier approach detailed in Part I to the study of correlations. In particular, with this model, we are able to derive compact expressions of the displacement and stress correlations in the general case of anisotropic elasticity. In the specific case of an elastically isotropic medium, the equations become tractable analytically. In particular, we find strongly anisotropic correlations for the displacement field, which decay as $1/d^3$ in the longitudinal direction (for instance, correlations along the x axis of displacements in the x direction) and as $1/d$ in the transverse direction (for example, correlations along the y or z axis of displacements in the x direction). For the shear stress correlations, we recover the $1/d^3$ decay demonstrated by Lemaître but with an unexpected anisotropy in the sign of the correlations. Predictions of the model are validated by direct comparison with molecular statics calculations in model Lennad-Jones and $Al_{0.5}Mg_{0.5}$ alloys.

1. Microelasticity model

The microelasticity model of a random alloy is described in details in section 1 of Part I [17]. We only recall here the main ingredients and the reader is referred to Part I for details. We consider a substitutional alloy of N_{elem} elements. Each atom is modeled as an elastic inclusion located at its site in the crystalline lattice and embedded in a homogeneous elastic medium of elastic constants C_{ijkl}. The eigenstrain associated to each species is diagonal and expressed as $\overline{\overline{\varepsilon}}^{00}_{\alpha} = \varepsilon_{\alpha}\mathrm{diag}(1,1,1)$. The inclusions are assumed to be placed on a crystalline lattice in a system of volume $V = L_x L_y L_z$ that contains N atoms/inclusions. The atomic volume is $v_{at} = V/N$.

Every element is associated with a site occupancy random variable given by a Bernoulli distribution independent of the lattice site. The probability of site n to host an atom of type α is:

$$P_{\alpha}(n) = \begin{cases} 0 & \text{with probability } 1 - c_{\alpha} \\ 1 & \text{with probability } c_{\alpha} \end{cases}, \tag{2}$$

where c_α is the atomic concentration of element α in the random alloy. We insist on the fact that with this definition of $P_\alpha(n)$, we do not consider any ordering that may appear in real alloys [36, 37].

The eigenstrain ε_α associated to each species is defined with respect to a reference frame. In line with Part I and other theoretical studies on HEA [33, 38], we choose the reference frame as the lattice of the average alloy, defined such that the eigenstrains have a zero mean:

$$\sum_{\alpha=1}^{N_{elem}} c_\alpha \varepsilon_\alpha = 0. \tag{3}$$

The last ingredient of the model is a Gaussian spreading of the eigenstrains around each lattice site. The spreading function is:

$$f(\boldsymbol{r}) = \frac{v_{at}}{(2\pi)^{3/2} a^3} \exp\left(-\frac{\boldsymbol{r}^2}{2a^2}\right), \tag{4}$$

where the width of the gaussian function, a, is the spreading parameter. Noting $\{\boldsymbol{R_n}\}_{n=1,N}$ the atomic/inclusion positions on the lattice, the inclusion field of element α, $\theta_\alpha(\boldsymbol{r})$, is:

$$\theta_\alpha(\boldsymbol{r}) = \sum_{n=1}^{N} P_\alpha(n) f(\boldsymbol{r} - \boldsymbol{R_n}). \tag{5}$$

Based on this inclusion field, the microelasticity theory [17, 19, 20] yields closed-form expressions of the displacement and stress fields:

$$u_i(\boldsymbol{r}) = \sum_{\alpha=1}^{N_{elem}} \varepsilon_\alpha \sum_{\boldsymbol{K}\neq 0} \Lambda_i(\boldsymbol{K}) \tilde{\theta}_\alpha(\boldsymbol{K}) e^{i\boldsymbol{K}.\boldsymbol{r}} \tag{6}$$

$$\sigma_{ij}(\boldsymbol{r}) = \sum_{\alpha=1}^{N_{elem}} \varepsilon_\alpha \sum_{\boldsymbol{K}\neq \boldsymbol{0}} \left(\Xi_{ij}(\boldsymbol{K}) - C_{ijkl}\delta_{kl}\right) \tilde{\theta}_\alpha(\boldsymbol{K}) e^{i\boldsymbol{K}.\boldsymbol{r}} \tag{7}$$

where $\tilde{\theta}_\alpha(\boldsymbol{K})$ is the Fourier transform of $\theta_\alpha(\boldsymbol{r})$, $\boldsymbol{K} = 2\pi(n_x/L_x, n_y/L_y, n_z/L_z)$ are reciprocal space vectors (with $(n_x, n_y, n_z) \in \mathbb{Z}^3$). $\Lambda_i(\boldsymbol{K}) = -iG_{ij}(\boldsymbol{K})K_l C_{jlmm}$ and $\Xi_{ij}(\boldsymbol{K}) = C_{ijkl}G_{kp}(\boldsymbol{K})K_q K_l C_{pqmm}$ are interaction kernels for the displacements and stresses, functions of the Green's function for elasticity $G_{ij}(\boldsymbol{K})$. We use these expressions in the following sections to derive spatial correlations.

2. Displacement field correlations

2.1. General expression

We first discuss the spatial correlations of the displacement field expressed as a 3×3 tensorial field, $\overline{\overline{U}}(\boldsymbol{d})$. The component

$$U_{ij}(\boldsymbol{d}) = \langle u_i(\boldsymbol{r})\overline{u_j(\boldsymbol{r}+\boldsymbol{d})}\rangle, \tag{8}$$

is the correlation between the displacements in directions i and j of material points separated by a vector $\boldsymbol{d}$. Brackets $\langle\ .\ \rangle$ denote an average over space and realizations of the random inclusion field. Note that, as in Part I, the spatial average is performed over the continuum space and not just at the atomic positions. After averaging, we obtain:

$$U_{ij}(\boldsymbol{d}) = \sum_{\boldsymbol{K}\neq 0} \Lambda_i(\boldsymbol{K})\overline{\Lambda_j(\boldsymbol{K})} \left[\sum_{\alpha=1}^{N_{elem}} \sum_{\beta=1}^{N_{elem}} \varepsilon_\alpha \varepsilon_\beta \langle \tilde{\theta}_\alpha(\boldsymbol{K}) \overline{\tilde{\theta}_\beta(\boldsymbol{K})} \rangle \right] \exp\left(i\boldsymbol{K}.\boldsymbol{d}\right). \tag{9}$$

Information relative to the occupancy of the lattice sites is contained in the term between square brackets that can be expressed as a function of the alloy composition as shown in Appendix A of Part I:

$$\sum_{\alpha=1}^{N_{elem}} \sum_{\beta=1}^{N_{elem}} \varepsilon_\alpha \varepsilon_\beta \langle \tilde{\theta}_\alpha(\boldsymbol{K}) \overline{\tilde{\theta}_\beta(\boldsymbol{K})} \rangle = \frac{v_{at}\Delta\varepsilon^2}{V} \exp(-a^2\boldsymbol{K}^2), \tag{10}$$

where we have introduced the variance of the eigenstrains:

$$\Delta\varepsilon^2 = \sum_{\alpha}^{N_{elem}} c_\alpha \varepsilon_\alpha^2. \tag{11}$$

Combining Eqs. (9) and (10), we find

$$U_{ij}(\boldsymbol{d}) = \frac{v_{at}\Delta\varepsilon^2}{V} \sum_{\boldsymbol{K}\neq 0} \Lambda_i(\boldsymbol{K})\overline{\Lambda_j(\boldsymbol{K})} \exp\left(i\boldsymbol{K}.\boldsymbol{d} - a^2\boldsymbol{K}^2\right). \tag{12}$$

Finally, considering the limit of an infinite volume with $L_x, L_y, L_z \to +\infty$, the discrete sum can be replaced by an integral, yielding:

$$U_{ij}(\boldsymbol{d}) = \frac{v_{at}\Delta\varepsilon^2}{(2\pi)^3} \int \boldsymbol{dK}\ \Lambda_i(\boldsymbol{K})\overline{\Lambda_j(\boldsymbol{K})} \exp\left(i\boldsymbol{K}.\boldsymbol{d} - a^2\boldsymbol{K}^2\right). \tag{13}$$

In an anisotropic elastic medium, this integral can be solved numerically to yield displacement correlations for a given $\boldsymbol{d}$. In the case of isotropic elasticity, the elastic kernel reduces to $\Lambda_i(\boldsymbol{K}) = -i\frac{1+\nu}{1-\nu}\frac{K_i}{\boldsymbol{K}^2}$ [20], such that:

$$U_{ij}(\boldsymbol{d}) = \frac{v_{at}\Delta\varepsilon^2}{(2\pi)^3} \left(\frac{1+\nu}{1-\nu}\right)^2 \int \boldsymbol{dK} \frac{K_i K_j}{\boldsymbol{K}^4} \cos(\boldsymbol{K}.\boldsymbol{d}) \exp\left(-a^2\boldsymbol{K}^2\right), \tag{14}$$

where $\exp(i\boldsymbol{K}.\boldsymbol{d})$ was replaced by $\cos(\boldsymbol{K}.\boldsymbol{d})$ because of the symmetry of the integrand. Due to the isotropy of the medium, the correlation tensor can be expressed in terms of only two correlation functions, between either longitudinal or transverse displacements. To show this, we start by considering the displacement correlations along a given axis.

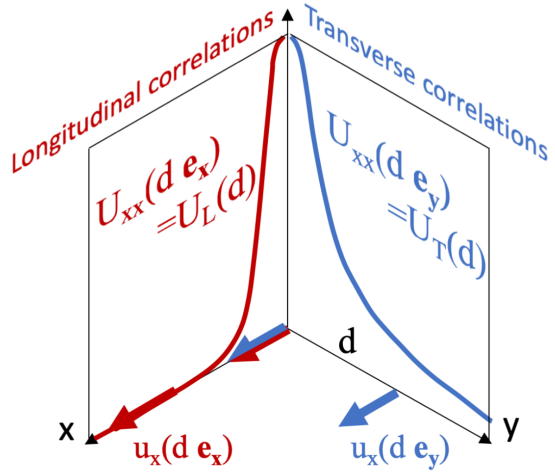

Figure 1. Graphical illustration of transverse and longitudinal displacement correlations.

2.2. Correlations along an axis

Let us first assume that $\boldsymbol{d}$ is along an axis of the material frame noted $(\boldsymbol{e_x}, \boldsymbol{e_y}, \boldsymbol{e_z})$. Since the medium is isotropic, we can choose $\boldsymbol{d}$ along the z axis, such that:

$$U_{ij}(d\boldsymbol{e_z}) = \frac{v_{at}\Delta\varepsilon^2}{(2\pi)^3}\left(\frac{1+\nu}{1-\nu}\right)^2 \int \boldsymbol{dK}\frac{K_iK_j}{\boldsymbol{K}^4}\cos(K_z.d)\exp\left(-a^2\boldsymbol{K}^2\right). \tag{15}$$

If $i \neq j$, either i or j is different from z. The integrand is then odd with respect to the corresponding K-component and $U_{ij}(d\boldsymbol{e_z}) = 0$. The correlation tensor is thus diagonal along the z axis of the material frame. Because of the isotropy of the medium, this remains true for any axis: displacements along orthogonal directions are not correlated along either direction, nor along the third perpendicular direction.

The diagonal terms of $\overline{\overline{U}}$ contain auto-correlation functions. As illustrated in Fig. 1, we need to distinguish the correlations between longitudinal displacements, for instance $U_{xx}(d\boldsymbol{e_x})$, e.g. the correlation along the x axis of displacements in the x direction (illustrated in red in Fig. 1), and the correlations between transverse displacements, for instance $U_{xx}(d\boldsymbol{e_y})$. We start with the correlations between longitudinal displacements denoted $U_L(d)$, which are the same along any axis of the medium because of its isotropy: $U_L(d) = U_{xx}(d\boldsymbol{e}_x) = U_{yy}(d\boldsymbol{e_y}) = U_{zz}(d\boldsymbol{e_z})$. It is shown in Appendix A.2 that in this case, the integral in Eq. (15) can be carried out analytically, yielding:

$$U_L(d) = 4\langle u^2\rangle\left(\frac{a}{d}\right)^3\left[\frac{\sqrt{\pi}}{2}\mathrm{erf}\left(\frac{d}{2a}\right) - \frac{d}{2a}\exp\left(-\frac{d^2}{4a^2}\right)\right], \tag{16}$$

where $\langle u^2\rangle$ is the variance of the displacement field. In Part I, we showed:

$$\langle u^2\rangle = \frac{v_{at}\Delta\varepsilon^2}{4\pi^{3/2}a}\left(\frac{1+\nu}{1-\nu}\right)^2. \tag{17}$$

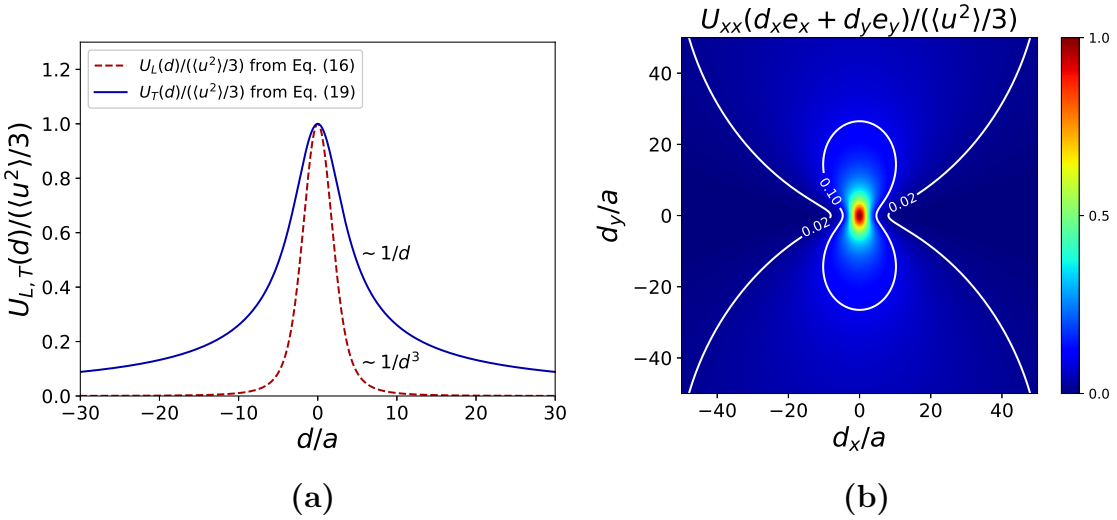

Figure 2. (a) Normalized transverse and longitudinal displacement correlations U_T and U_L. (b) Normalized displacement correlations U_{xx} in the (x, y) plane. White lines represent contour lines at 0.1 and 0.02 to highlight the anisotropy of the spatial correlations.

Eq. (16) is shown as a dashed red line in Fig. 2.a. We note that the Gaussian spreading of the inclusions prevents the divergence of the auto-correlation function at the origin and as expected, $U_L(0) = \langle u^2\rangle/3$ (because $\langle u^2\rangle/3 = \langle u_z^2\rangle = \langle u_y^2\rangle = \langle u_x^2\rangle$ due to the isotropy of the system). The far-field behavior of Eq. (16) is obtained by taking the limit $d \gg a$ where $\mathrm{erf}(d/2a) \to 1$, such that

$$U_L(d) \underset{d\gg a}{=} 2\sqrt{\pi}\langle u^2\rangle \left(\frac{a}{d}\right)^3, \tag{18}$$

showing that the correlation between longitudinal displacements decreases as $1/d^3$ at long range.

The second case is the correlation between transverse displacements, for instance U_{xx} along the y axis as shown in blue on Fig 1. By symmetry, correlations are the same for all $U_{ii}(d_j \boldsymbol{e_j})$ with $i \neq j$ and this remain true for the transverse displacements to any axis of the medium. We note this transverse correlation function $U_T(d)$. Following the same steps as in Appendix A.2, we obtain:

$$U_T(d) = \langle u^2\rangle \frac{a}{d}\left[\frac{\sqrt{\pi}}{2}\left(1 - \frac{2a^2}{d^2}\right)\mathrm{erf}\left(\frac{d}{2a}\right) + \frac{a}{d}\exp\left(-\frac{d^2}{4a^2}\right)\right]. \tag{19}$$

Taking the limit $d \gg a$ we find:

$$U_T(d) \underset{d\gg a}{=} \frac{\sqrt{\pi}}{2}\langle u^2\rangle \left(\frac{a}{d}\right), \tag{20}$$

showing a $1/d$ decay. Eq. (19) is drawn as a full blue line in Fig. 2.a and clearly shows the different scaling behaviors of the longitudinal and transverse correlations. Interestingly, the transverse correlations decrease much more slowly than the longitudinal correlations.

We insist that, because of the isotropy of the medium, $U_L(d)$ represents the correlations between longitudinal displacements along any axis of the medium, while $U_T(d)$ is the correlation between any transverse displacement along any axis of the medium.

2.3. Correlations in a plane

We can now consider the correlations between displacements in a plane, for instance the auto-correlation of u_x or u_y or cross-correlations between u_x and u_y in the (x, y) plane. Using a planar rotation and the fact that cross-correlations are zero along any frame axis, we find:

$$U_{xx}(d_x\boldsymbol{e_x} + d_y\boldsymbol{e_y}) = U_L(d)\cos^2(\theta) + U_T(d)\sin^2(\theta) \tag{21}$$

$$U_{xy}(d_x\boldsymbol{e_x} + d_y\boldsymbol{e_y}) = (U_L(d) - U_T(d))\sin(\theta)\cos(\theta) \tag{22}$$

where $d = \sqrt{d_x^2 + d_y^2}$ and $\theta = \arctan(d_y/d_x)$. Fig. 2.b displays Eq. (21) as a color map with contour lines, again showing the strikingly different long-range behaviors in the longitudinal and transverse directions.

We note, although this will not be detailed here, that the same reasoning can be generalized to three dimensions to yield the displacement correlations between any two material points in space.

3. Shear stress field correlations

The spatial correlations of the stress field is represented by a fourth-order tensor whose components are defined as:

$$\Sigma_{ij,mn}(\boldsymbol{d}) = \langle \sigma_{ij}(\boldsymbol{r})\overline{\sigma_{mn}(\boldsymbol{r}+\boldsymbol{d})}\rangle. \tag{23}$$

Considering Eq. (7) and following the same steps as in the previous section, we obtain in the limit of an infinite medium:

$$\Sigma_{ij,mn}(\boldsymbol{d}) = \frac{v_{at}\Delta\varepsilon^2}{(2\pi)^3}\int \boldsymbol{dK}\ \left(\Xi_{ij}(\boldsymbol{K}) - C_{ijkl}\delta_{kl}\right)\left(\Xi_{mn}(\boldsymbol{K}) - C_{mnpq}\delta_{pq}\right)\cos(\boldsymbol{K}\cdot\boldsymbol{d})\exp\left(-a^2\boldsymbol{K}^2\right). \tag{24}$$

In an isotropic elastic medium, the interaction kernel reduces to $\Xi_{ij}(\boldsymbol{K}) = 2\mu\left(\frac{1+\nu}{1-\nu}\right)K_iK_j/\boldsymbol{K}^2$. As in Part I, we will focus on the shear components that are relevant because they form the structural stress noise impeding dislocation motion. Considering the isotropic case, $C_{ijkl}\delta_{kl} = 0$, the correlation function between shear stresses ($i \neq j$ and $m \neq n$) reduces to:

$$\Sigma_{ij,mn}(\boldsymbol{d}) = \frac{v_{at}\Delta\varepsilon^2}{(2\pi)^3}4\mu^2\left(\frac{1+\nu}{1-\nu}\right)^2\int \boldsymbol{dK}\ \frac{K_iK_jK_mK_n}{K^4}\ \cos(\boldsymbol{K}\cdot\boldsymbol{d})\exp\left(-a^2\boldsymbol{K}^2\right) \tag{25}$$

In the following, we will consider correlations along an axis and then in a plane.

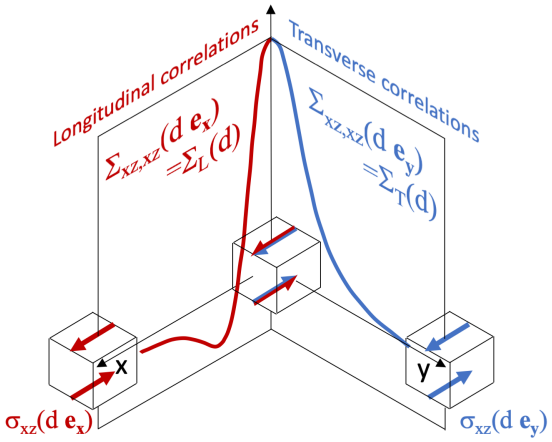

Figure 3. Graphical illustration of transverse and longitudinal shear stress correlations in the (x, y) plane.

3.1. Correlations along an axis

If $\boldsymbol{d}$ is along an axis, for instance the z axis, then if $(i, j) \neq (m, n)$, the integrand of Eq. (25) is necessarily odd with respect to two K-components and $\Sigma_{ij,mn}(d\boldsymbol{e_z}) = 0$. We thus focus on the auto-correlation terms, $\Sigma_{ij,ij}(d\boldsymbol{e_z})$. As for the displacements, we need to distinguish between transverse and longitudinal correlations. As illustrated in Fig. 3, transverse correlations are for instance the auto-correlation of σ_{xz} along the y axis, which by symmetry is the same for all σ_{ij} stresses along k axes with $i \neq j \neq k$. We will note this correlation function $\Sigma_T(d)$. Longitudinal correlations are for instance the auto-correlation of σ_{xz} along the x axis, which by symmetry is the same for all σ_{ik} stresses along k axes with $i \neq k$. We note the latter $\Sigma_L(d)$. In Appendix A.3, we show that:

$$\Sigma_T(d) = 15\langle\tau^2\rangle \left(\frac{a}{d}\right)^3 \left[\sqrt{\pi}\left(1 - \frac{6a^2}{d^2}\right)\mathrm{erf}\left(\frac{d}{2a}\right) + \frac{6a}{d}\exp\left(-\frac{d^2}{4a^2}\right)\right], \tag{26}$$

with $\langle\tau^2\rangle$, the variance of the shear stresses that was derived in Part I:

$$\langle\tau^2\rangle = \frac{v_{at}\Delta\varepsilon^2\mu^2}{30\pi^{3/2}a^3}\left(\frac{1+\nu}{1-\nu}\right)^2. \tag{27}$$

As expected, Talyor expansions of the terms between brackets show that $\Sigma_T(0) = \langle\tau^2\rangle$. On the other hand, in the limit $d \gg a$, we have:

$$\Sigma_T(d) \underset{d\gg a}{=} 15\sqrt{\pi}\langle\tau^2\rangle \left(\frac{a}{d}\right)^3. \tag{28}$$

Similarly, we find for the longitudinal correlations:

$$\Sigma_L(d) = -30\langle\tau^2\rangle \left(\frac{a}{d}\right)^3 \left[\sqrt{\pi}\left(1 - \frac{12a^2}{d^2}\right)\mathrm{erf}\left(\frac{d}{2a}\right) + \frac{a}{d}\left(12 + \frac{d^2}{a^2}\right)\exp\left(-\frac{d^2}{4a^2}\right)\right], \tag{29}$$

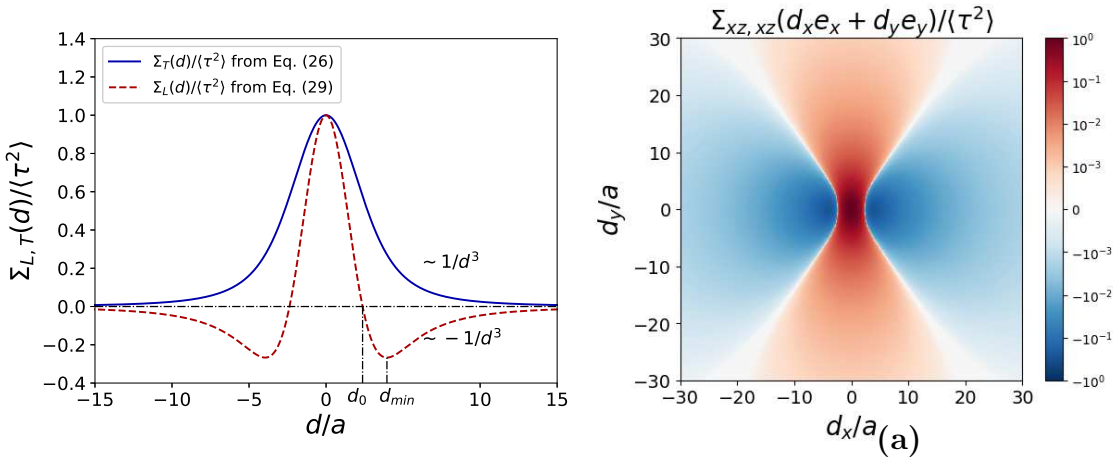

Figure 4. (a) Normalized transverse and longitudinal shear stress correlations, Σ_T and Σ_L (as examples, $\Sigma_T(d) = \Sigma_{xz,xz}(d\boldsymbol{e_y})$ and $\Sigma_L(d) = \Sigma_{xz,xz}(d\boldsymbol{e_x})$). (b) Stress correlations $\Sigma_{xz,xz}$ in the (x, y) plane plane in log scale.

which in the limit $d \gg a$ becomes:

$$\Sigma_L(d) \underset{d\gg a}{=} -30\sqrt{\pi}\langle\tau^2\rangle \left(\frac{a}{d}\right)^3. \tag{30}$$

Both Eqs. (28) and (30) display the same $1/d^3$ long-range behavior derived by Lemaître in a more general setting [31]. Interestingly, we evidence a striking difference between Σ_T and Σ_L illustrated in Fig. 4.a. While $\Sigma_T(d)$ is positive for all d, $\Sigma_L(d)$ is positive at short distance but becomes negative at longer distance. The cross-over between positive and negative correlations depends only on the spreading parameter a and is found numerically to be $d_0 \simeq 2.4a$. Moreover, Σ_L displays a minimum at $d_{min} \simeq 4a$ for which the correlation is negative. This negative correlation translates into an intrinsic length scale $\lambda \simeq 8a$ in the noisy stress environment.

3.2. Correlations in a plane

As for the displacements, we can express the stress correlations in a plane as a function of only Σ_L, Σ_T using polar coordinates. We will discuss here only the case of the auto-correlation of σ_{xz} in the (x, y) plane. We chose this particular correlation because of its relevance for the plastic behavior of an alloy. Indeed the σ_{xz} stress is the stress component which impedes the motion in the (x, y) plane of a dislocation with a Burgers vectors along the x axis, i.e. both a screw dislocation along the x axis and an edge dislocation along the y axis. Using a rotation in the plane and the fact that cross-correlations are zero along the frame axes, we find a similar expression as for the displacements:

$$\Sigma_{xz,xz}(d_x\boldsymbol{e_x} + d_y\boldsymbol{e_y}) = \Sigma_L(d)\cos^2(\theta) + \Sigma_T(d)\sin^2(\theta). \tag{31}$$

Fig. 4.b displays the stress correlation of Eq. (31) in the (x, y) plane using a log-scale color map in order to reveal the positive and negative stress correlation regions. Other correlation terms in the plane and in the 3D space can be obtained using similar calculations.

In brief, we have shown in this section that the Fourier-based microelasticity model can be used to derive closed-form expressions for the displacement and shear stress correlations in the general case. In the specific case of isotropic elasticity, we derived analytical expressions for the spatial correlations of the displacement and stress field emerging in a random alloy. We will now test these expressions by comparison with atomistic calculations.

4. Molecular statics calculations

The expressions derived in sections 2 and 3 rely on assumptions concerning a continuum approximation, the isotropy of the elastic medium and the representation of atoms of different nature as dilatational eigenstrains. When dealing with real systems, these assumptions might appear questionable since short-range effects, chemical effects, or anisotropic eigenstrains and elasticity might dominate. Therefore, it is important to test the predictions of the elastic model by comparison with atomistic systems. To this end, we performed molecular statics calculations in a model Lennard-Jones system and an $Al_{0.5}Mg_{0.5}$ alloy, that, as shown in Part I [17], compare well with predictions of our elastic model for the variance of the displacement and stress fields. All atomistic calculations were performed with Lammps software [39].

The elastic parameters of both systems have been computed and are listed in Tab. 1. The Bacon-Scattergood average [40, 41] is used to compute isotropic parameters from cubic elastic constants.

The correlations functions obtained in sections 2 and 3 depend on the Gaussian spreading parameter a. In Part I [17], we have shown that this quantity can be determined such that the variance of displacements and stresses obtained with the Fourier approach match the prediction of the real-space approach that do not rely on any fitting parameter (see Eq. (19) and (24) of Part I). This approach yields two different parameters a_u and a_τ (see Tab. 1) obtained respectively from the variance of the displacement and stress field.

	$\bar{a}_{lat}$(Å)	v_{at}(Å^3)	a_u(Å)	a_τ(Å)	A	μ (GPa)	ν	$\Delta\varepsilon^2$
LJ $A_{0.5}B_{0.5}$	3.982	15.79	1.12	0.903	2.65	171.1	0.345	$3.66 \cdot 10^{-6}$
EAM $Al_{0.5}Mg_{0.5}$	4.282	19.6	1.199	0.971	0.95	20.7	0.331	$3.41 \cdot 10^{-3}$

Table 1. Average properties of the Lennard-Jones $A_{0.5}B_{0.5}$ and $Al_{0.5}Mg_{0.5}$ random alloys: $\bar{a}_{lat}$ is the lattice parameter of the average alloy, v_{at} the corresponding atomic volume, a_u and a_τ are the Gaussian spreading parameters for the displacements and stresses, $A = 2C_{44}/(C_{11} - C_{12})$ the Zener anisotropy cofficient, μ and ν the isotropic elastic constants and $\Delta\epsilon^2$ the variance of the eigenstrains.

4.1. Lennard-Jones model $A_0.5B_0.5$ alloy

We first consider a FCC binary alloy $A_{0.5}B_{0.5}$ modeled with the shifted Lennard-Jones (LJ) interatomic potential described in Part I [17]. This model system holds the advantage of introducing a small and well-controlled size effect through the amplitude of the shifted potential while reducing non-linear effects to a minimum. However, the elastic anisotropy of this system is quite large (the Zener anisotropic coefficient is $A = 2.65$ as reported in Tab. 1).

Displacement correlations. To investigate correlations in this system, we constructed random $A_{0.5}B_{0.5}$ FCC lattices of size $(160\bar{a}_{lat})^3$ and relaxed the atomic positions with 3D periodic boundary conditions. To reach sufficient statistics, we used ten independent simulations and averaged the correlations over realizations and over crystallographically equivalent directions. Fig. 5.a shows the transverse correlation, $U_T(d)$, along the $\langle 100 \rangle$ direction of the FCC lattice (for instance $U_{xx}(d\boldsymbol{e_y})$ with $x = [100]$ and $y = [010]$). The atomistic results match very well the analytic prediction of Eq. (19). As shown in the inset, the atomistic calculations display the $1/d$ behavior predicted by Eq. (20) over more than one decade. The small difference seen at large distances is attributed to a finite size effect demonstrated in Fig. 6, which compares correlations computed in systems of different sizes.

Fig. 5.b shows the longitudinal correlation, $U_L(d)$, along the $\langle 100 \rangle$ direction (for instance $U_{xx}(d\boldsymbol{e_x})$ with $x = [100]$), compared with the prediction of the elastic model. While the elastic model predicts positive correlations decreasing as $1/d^3$, the correlations obtained from the model LJ system drop abruptly to a small and negative value and remains slightly negative at all distances. This difference is attributed to the anisotropic elasticity of the LJ system (Zener coefficient $A = 2.65$), which is the main approximation of the elastic model compared to this when simple atomic system. We should also keep in mind that Figs. 5.a and b are predictions without fitting parameters since the only free parameter of the model, a, was chosen based on the real-space approach. The overall agreement is therefore satisfactory and shows the adequacy of the elastic model.

Fig. 5.c shows the correlations in the (x, y) plane of displacements u_x, with $x = [100]$ and $y = [010]$. Despite the discrepancy of the correlations along the x axis discussed earlier, this map agrees very well with the analytical prediction shown in Figs. 2.b. We recover in particular the slowly decreasing correlations along the transverse y axis and rapidly decreasing correlations along the longitudinal x axis.

Such anisotropy between transverse and longitudinal correlations was reported by Glas [24] in an atomistic model of semiconductor. We note however that in his study, longitudinal and transverse correlations share similarities with the results reported here. The difference between the numerical results from Glas and the ones reported here may be attributed to the specific features of the interatomic potential employed to model covalent bonds in Ref. [24] or also to strong finite size effects associated with small simulations cell employed in his study.

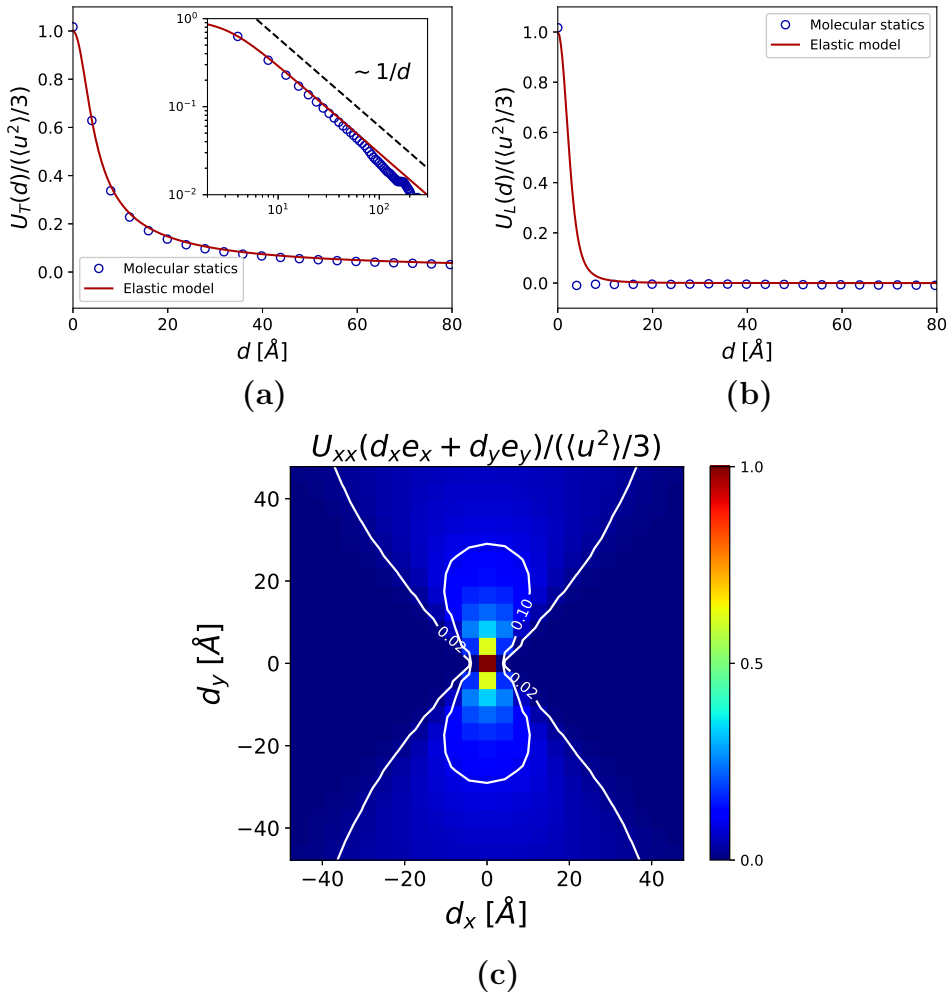

Figure 5. Transverse (a) and longitudinal (b) displacement correlations obtained from atomistic calculations in a Lennard-Jones $A_{0.5}B_{0.5}$ system (circles) and from the elastic model (full lines). The inset in panel (a) shows the same plot with a log-log scale. (c) Spatial correlations U_{xx} in the (x, y) plane.

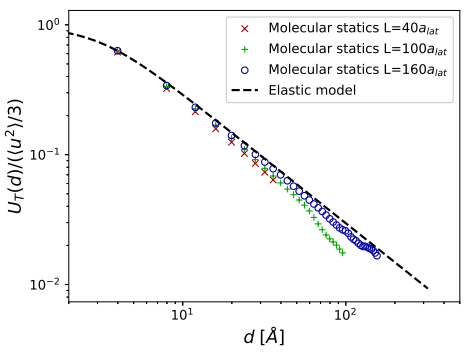

Figure 6. Finite size effect: transverse displacement correlations in systems of different sizes. L denotes the linear size of the cubic simulation cell.

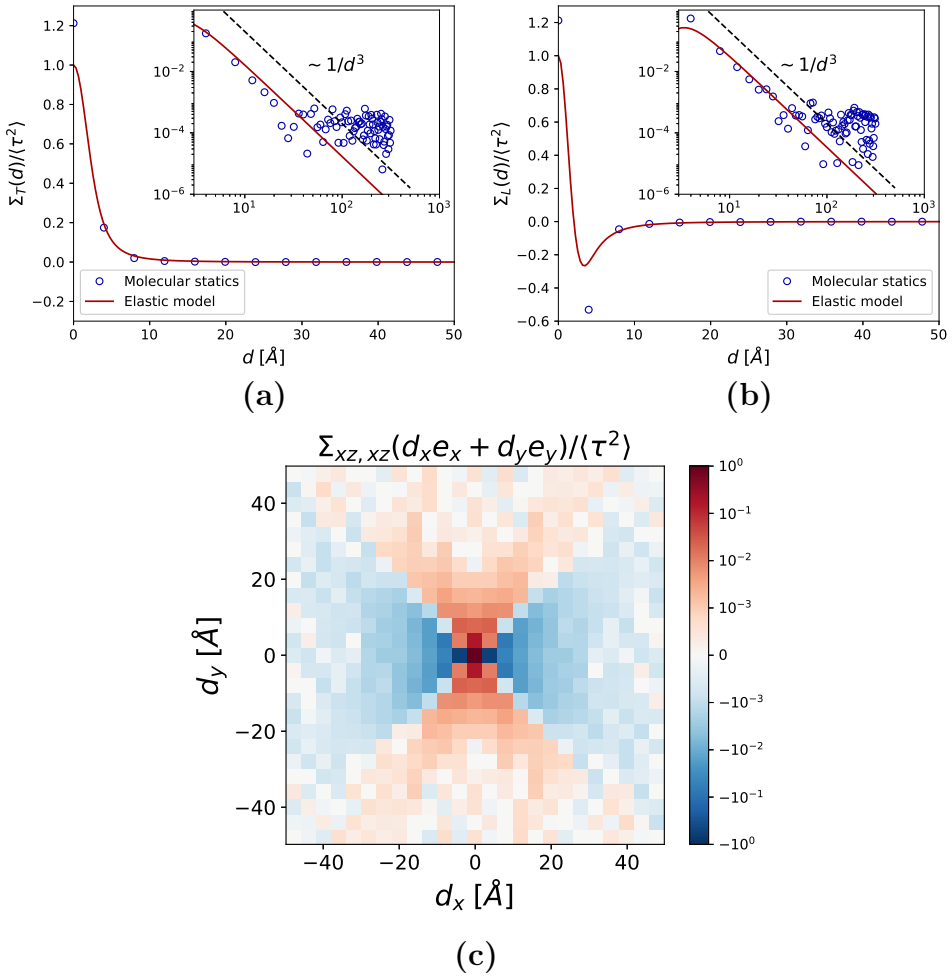

Figure 7. (a) Transverse and (b) longitudinal shear stress correlations obtained from atomistic calculations in a Lennard-Jones $A_{0.5}B_{0.5}$ system (circles) and from the elastic model (full lines). The insets display the same data with a log-log scale (absolute value is taken in case of negative quantities). (c) Spatial correlations $\Sigma_{xz,xz}$ in the (x, y) plane.

Shear stress correlations. To evaluate the correlations between shear stresses, we computed the atomic virial stresses in the relaxed configurations. The results, averaged over ten independent simulations and between equivalent directions are summarized in Fig. 7. As for the displacements, the free parameter a_τ (see Tab. 1) was chosen such that the variance of the stress matches the results of the real space method (see Part I [17]).

We see in Figs. 7.a and b that the atomistic calculations matches qualitatively the predictions of the elastic model with positive transverse correlations and negative longitudinal correlations. In addition, the log-log plots in the insets show that the atomistic correlations follow the expected $1/d^3$ power-law decay predicted by the elastic model (see Eq. (28) and Eq. (30)).

We note that the elastic model does not reproduce exactly the variance of the stress

(i.e. the correlations in $d = 0$) and the magnitude of the negative correlation obtained at $d = a_{lat}$ in Fig. 7.b. These discrepancies are attributed to the anisotropic elasticity of the model LJ system and the inaccuracy of the virial stress to estimate stresses at the atomic level [42, 43, 44].

Fig. 7.c displays the stress correlation map of $\Sigma_{xz,xz}$ in the (x, y) plane with a log scale, dividing the plane into positive (red) and negative (blue) correlation regions. Again, these correlations match well the prediction obtained from the elastic model shown in Fig. 4.c.

4.2. $Al_{0.5}Mg_{0.5}$ alloy

We consider now a binary $Al_{0.5}Mg_{0.5}$ random alloy modeled with the EAM potential of Liu et al. [45]. This binary system holds the advantage of involving species of different radii but of similar chemistry, with a weak elastic anisotropy (see Tab. 1). In addition, the eigenstrain tensor associated with both species can be identified with dilatational inclusions, matching well the assumptions of the model.

Displacement correlations. Fig. 8 shows that the transverse correlation, $U_T(d)$, follows the $1/d$ behavior as predicted by Eq. (20) over more than one decade. As for the LJ system, the discrepancy obtained at large distances is due to a finite size effect. Fig. 8.b shows the longitudinal correlation, $U_L(d)$, compared with the prediction of the elastic model. We find that, in agreement with the model, the longitudinal correlation in Fig. 8.b decreases much faster than the transverse correlation in Fig. 8.a. The decrease is however slightly slower than the $1/d^3$ behavior expected from the model. This difference may be due to the weak anisotropy of the atomistic alloy or to chemical effects. Fig. 8.c displays the correlations in the (x, y) plane of displacements in x direction, with $x = [100]$ and $y = [010]$, showing again a very good agreement with the predicted map of Fig. 2.b

Shear stress correlations. The stress correlations are evaluated from the atomic virial stresses obtained in the relaxed configurations. The results are summarized in Fig. 9. The atomistic results reported in Figs. 9.a show a good agreement between the atomistic results and the prediction of the elastic model. The log-log plots in the insets show a remarkable agreement over more than one decade between the atomistic results and the expected $1/d^3$ power-law decay predicted by the elastic model (see Eq. (28) and Eq. (30)). Fig. 9.c displays the stress correlation map of $\Sigma_{xz,xz}$ in the (x, y) plane with a log scale and matches very well the prediction obtained from the elastic model shown in Fig. 4.c.

Overall, both the LJ and $Al_{0.5}Mg_{0.5}$ random binary alloys reproduce all the features of the displacement and stress correlations predicted analytically by our elastic model. Some features such as the positive longitudinal displacement correlations and the long-range $1/d^3$ stress correlations are better captured with the Al-Mg alloy, which is probably a consequence of the weak elastic anisotropy of this system compared to the LJ alloy.

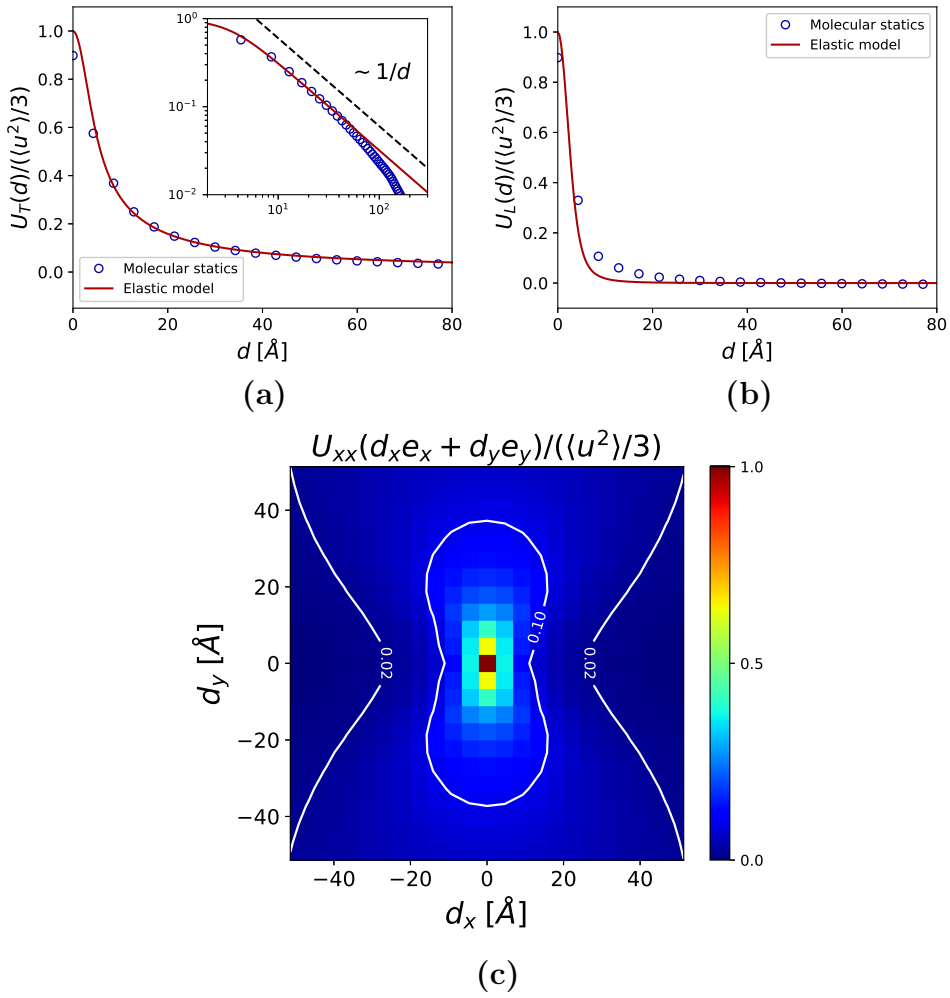

Figure 8. Transverse (a) and longitudinal (b) displacement correlations obtained from atomistic calculations in $Al_{0.5}Mg_{0.5}$ (circles) and from the elastic model (full lines). The inset in panel (a) shows the same plot with a log-log scale. (c) Spatial correlations U_{xx} in the (x, y) plane.

The agreement obtained in this section also reveals that the effect of the crystalline lattice (neglected in the Fourier-based elastic model because of the spatial average) remains limited. This can be understood by noting that the displacement and stress correlation functions vary smoothly and involve wave-lengths larger than the interatomic distance.

5. Discussion

Using a microelasticity model in Fourier space, we have obtained analytic expressions of the correlation functions of displacements and stresses in a random alloy. We find that, even if the alloy is fully disordered and elastically isotropic, correlations are highly anisotropic, with different scaling behaviors for the transverse and longitudinal displacement correlations, and the same scaling but different signs for the transverse

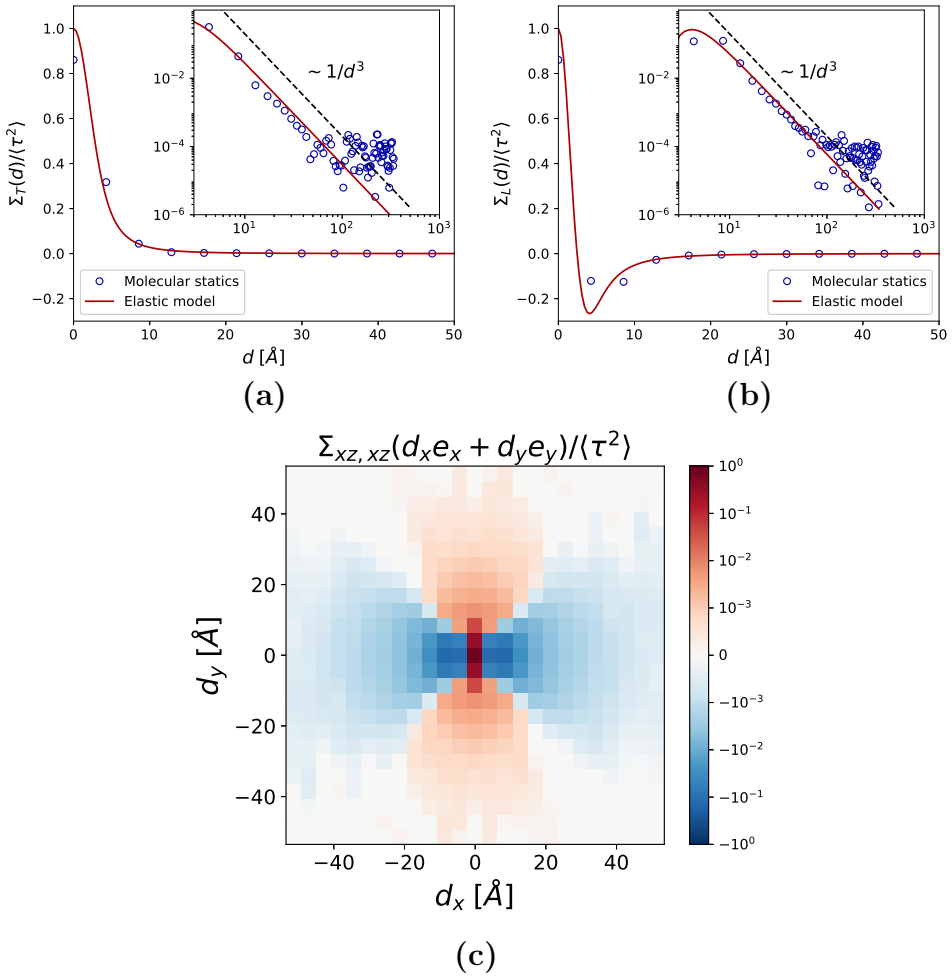

Figure 9. (a) Transverse and (b) longitudinal shear stress correlations obtained from atomistic calculations in $Al_{0.5}Mg_{0.5}$ (circles) and from the elastic model (full lines). The insets display the same data with a log-log scale (absolute value is taken in case of negative quantities). (c) Spatial correlations $\Sigma_{xz,xz}$ in the (x, y) plane.

and longitudinal shear stress correlations. We used a continuous approach where the displacements and stresses are averaged everywhere in the continuum space and not just at the atomic positions. A consequence is that the correlation functions obtained here do not depend on the crystalline lattice. The real space approach introduced in Part I can be extended to express discrete correlation functions between atomic displacements and stresses, which depend on the crystal lattice. In this case, the expressions involve an infinite sum over the crystalline lattice that can not be solved analytically. However, we checked numerically that the resulting correlation functions exhibit the same spatial dependence as the continuous correlations discussed here. This shows the suitability of the present continuous approximation, as also attested by the comparison with atomistic calculations performed in section 4.

Correlations in displacements and stresses are interesting in their own rights. We discuss them in turn below.

5.1. Finite size effects

As demonstrated theoretically in section 2 and numerically for specific systems in section 4, the transverse displacement correlations decrease as $1/d$. An implication of this long-range behavior concerns the influence of the system size on atomistic simulation results. In particular, the use of a finite system size with periodic boundary conditions necessarily truncates these long-range correlations as shown in Fig. 6, which in turn affects quantities such as the mean-square displacement.

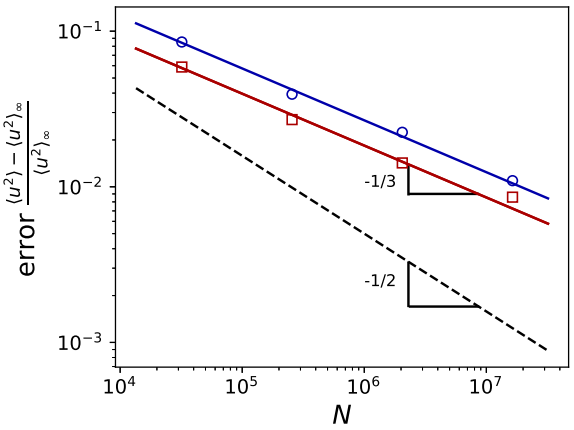

Figure 10. Error on the mean-square displacement $\langle u^2\rangle$ due to finite size effects in the Lennard-Jones $A_{0.5}B_{0.5}$ (squares) and the $Al_{0.5}Mg_{0.5}$ alloy (circles) as a function of system size. The converged values, $\langle u^2\rangle_\infty$, were obtained by extrapolation following the $1/N^{1/3}$ convergence highlighted by the continuous lines. The dashed line shows a $1/\sqrt{N}$ trend expected in the case of uncorrelated displacements (central-limit theorem).

To evidence these finite size effects, Fig. 10 displays the error on the measured mean-square displacement with respect to the number of atoms in the simulation cell. If the atomic displacements were uncorrelated, one would expect the statistics to follow the central-limit theorem and to converge as $\simeq 1/\sqrt{N}$ (shown with a dashed black curve in Fig. 10). Both LJ and $Al_{0.5}Mg_{0.5}$ systems investigated in this article follow a slower convergence. The error decreases as $1/L \sim 1/N^{1/3}$ (continuous lines in Fig. 10) where L is the linear size of the system, a direct consequence of the transverse displacement correlations that also decrease as $1/d$. Therefore, the mean square displacements follow a geometric convergence, as observed in other problems involving elastic interactions [46].

We note that the mean square displacements discussed in Part I of this paper [17] were measured in large systems containing at least $1.6 \cdot 10^7$ atoms such that the finite size error remains of the order of 1%. The slow $1/N^{1/3}$ convergence implies however that the use of small simulation cells containing a few hundred atoms, as commonly employed in ab-initio calculations [13, 14, 15, 16], does not yield values of the mean-

square displacement representative of infinite systems, even if the results are averaged over different random configurations of the same alloy. The error depends on the system but could be of the order of 20% for 2048 atom systems and as high as 40% for a 256 atom systems. This observation might partly explain the discrepancies obtained in the litterature between ab-initio calculations, continuous modeling and experiments [13, 14, 15, 16].

By way of contrast, because stress correlations decrease with $1/d^3$, the mean square stresses do not exhibit strong finite size effects.

5.2. Displacement correlations and diffuse scattering

Displacement correlations have been mainly discussed in the literature with regards to diffuse scattering effects in X-ray and neutron diffraction experiments, and diffuse contrast in TEM. In his pioneering work, Huang [21] used a real-space continuum approach and modeled impurities as spherical Eshelby inclusions. He expressed the effect of a single isolated impurity on the scattering intensity and, remaining in the dilute solid solution limit, approximated the total scattered intensity as the sum of individual contributions. Later, Barabash et al. [22] showed by comparison with atomistic calculations that this continuum approach predicts accurately the intensity scattered by isolated impurities because of the dominant contribution of long wavelength displacements to Huang's diffuse scattering.

Thorpe et al. [23] extended the study of Huang scattering to concentrated alloys by including the effect of displacement correlations. They did not use a continuum approach but modeled a discrete random binary alloy with two types of spring-bonds between lattice sites. This model allows to define a Green's function [23] and thus bares strong similarities with the discrete real-space approach described in Part I.

Interestingly, the microelasticity model developed here can be used to extend Huang's continuum approach to concentrated alloys. Fully developing this line of work is out of the scope of the present article but an interesting prospect would be to compare predictions of such theory with results obtained in X-ray and neutron scattering experiments performed on complex HEA in order to analyse diffraction spectra in light of the displacement correlations discussed in this paper.

As noted in the literature [24, 47, 48], atomic displacements are affected by ordering of the chemical species in the alloy. For instance, it is obvious that no long-range displacement correlation can emerge from a perfectly ordered binary alloy (with a $L1_2$ or B_2 structure). In the intermediate case, one can investigate the role of composition fluctuations on the diffracted spectra by considering that the random occupancy variables $P_\alpha(n)$ are not independent of the lattice site, thus including short- or long-range orders [47, 48, 49]. Such line of work would be of interest for the study of HEA where chemical ordering remains an open question on many systems [36, 37, 50].

5.3. Stress correlations and dislocations

The spatial correlations of the shear stresses are central to assess the stress field acting on dislocations in random alloys. Indeed, as mentioned above, a dislocation with a Burgers vector along the x axis and gliding in the (x, y) plane is affected by Peach Koehler forces proportional to the σ_{xz} component of the stress tensor. A screw dislocation lying along the x axis will thus be sensitive to longitudinal stress correlations $\Sigma_L(d) = \Sigma_{xz,xz}(d\boldsymbol{e_x})$, while an edge dislocation lying along the y axis will feel transverse stress correlations $\Sigma_T(d) = \Sigma_{xz,xz}(d\boldsymbol{e_y})$. Given the differences in longitudinal and transverse correlations illustrated in Fig. 4, we expect that stresses in random alloy act differently on edge and screw dislocations.

A natural next step of this work is to combine the correlated stress environment discussed here with either a simple line tension model or a more advanced dislocation model accounting for long-range elasticity [35, 51, 52]. It will allow to assess the influence of stress correlations on the dislocation roughness (i.e. the shape of the dislocation line) and to clarify recent results obtained with atomistic calculations [53] and continuous modeling [35]. More importantly, it will allow to investigate the solid solution strengthening in concentrated alloys by estimating the critical stress to unpin a dislocation from the underlying correlated stress. In particular, this multi-scale approach will allow to relax some assumptions of average models [2, 32, 33] that rely on a unique dislocation length-scale to predict the critical resolved shear stress of the alloy.

Some efforts have been pursued in this direction by investigating dislocation roughening in a random stress environment [35] or the strengthening associated to stacking fault inhomogeneities [54]. However, the stress environment considered in these studies was simplified and did not incorporate stress correlations evidenced in this study.

In addition, one could consider combining this type of continuous model with saddle-point search methods [55, 56] to access thermally-activated processes and describe the strain-rate and temperature dependence of the plasticity in random alloys, that is very important to predict the temperature-dependent yield stress of the alloy.

6. Conclusion

In this two-part article, we have developed a continuum microelasticity model to investigate the statistical properties (variance and correlations) of the displacement and stress fields emerging in random alloys. In particular, we modeled a fully random alloy by considering occupancy probabilities independent of the lattice sites and only dependent on the species concentrations. Investigating the influence of short-range order or composition fluctuations on the displacement and stress correlations would therefore be a natural extension of this work.

We discussed above how displacement and stress correlations can be used to revisit theories of diffuse scattering and yield stress in random alloys. In the context of plasticity, the present random stress environment can be generated and implemented in

a dislocation dynamics framework [57, 58] to study for instance the competition between solid-solution and precipitation hardening in complex alloys. Beyond dislocations, any stress-induced microstructural process, such as the migration of twin interfaces [59] and other grain boundaries, could also be modeled in random alloys, accounting for the strong anisotropy of the correlations evidenced in the present study.

Acknowledgment

P.A.G and A.R. wish to acknowledge the financial support of IDEXLYON *Impulsion* project from the University of Lyon in the framework of the *Programme Investissements d'Avenir* (ANR-16-IDEX-005) grant from the University of Lyon IDEX. P.A.G also wishes to thank his wife for the quality time spend together during the Covid-19 lockdown.

Appendix A. Analytic computation of integrals

Appendix A.1. Some useful integrals

We note:

$$I_0 = \int_0^\infty dx \ \cos(bx)\exp(-ax^2) = \frac{1}{2}\sqrt{\frac{\pi}{a}}\exp\left(-\frac{b^2}{4a}\right) \tag{A.1}$$

and by differentiation:

$$\begin{aligned} I_2 &= \int_0^\infty dx \ x^2\cos(bx)\exp(-ax^2) \\ &= -\frac{\partial}{\partial a}\int_0^\infty dx \ \cos(bx)\exp(-ax^2) \\ &= \frac{\sqrt{\pi}}{4a^{3/2}}\left(1-\frac{b^2}{2a}\right)\exp\left(-\frac{b^2}{4a}\right). \end{aligned} \tag{A.2}$$

We also define the following integrals:

$$u_n(x) = \int_0^x dt \ t^n\exp(-t^2), \tag{A.3}$$

which can be computed by recurrence noting that $u_n(x) = \frac{n-1}{2}u_{n-2}(x) - \frac{x^{n-1}}{2}\exp(-x^2)$. We obtain:

$$u_0(d/2a) = \int_0^{d/2a} dt\ \exp(-t^2) = \frac{\sqrt{\pi}}{2}\mathrm{erf}(d/2a) \tag{A.4}$$

$$u_2(d/2a) = \int_0^{d/2a} dt\ t^2 \exp(-t^2) = \frac{1}{4}\left(\sqrt{\pi}\mathrm{erf}(d/2a) - \frac{d}{a}e^{-d^2/4a^2}\right) \tag{A.5}$$

$$u_4(d/2a) = \int_0^{d/2a} dt\ t^4 \exp(-t^2) = \frac{3}{8}\left(\sqrt{\pi}\mathrm{erf}(d/2a) - \frac{d}{a}\left(1+\frac{d^2}{6a^2}\right)e^{-d^2/4a^2}\right) \tag{A.6}$$

$$u_6(d/2a) = \int_0^{d/2a} dt\ t^6 \exp(-t^2) = \frac{15}{16}\left(\sqrt{\pi}\mathrm{erf}(d/2a) - \frac{d}{a}\left(1+\frac{d^2}{6a^2}+\frac{d^4}{60a^4}\right)e^{-d^2/4a^2}\right) \tag{A.7}$$

where $\mathrm{erf}(x) = \frac{2}{\sqrt{\pi}}\int_0^x dt\ \exp(-t^2)$ is the error function.

Appendix A.2. Computation of $U_L(d)$

Using spherical coordinates, such that $k = |\boldsymbol{K}|$ and ϕ and θ are the polar and azimuthal angles, we have:

$$\begin{aligned} K_x &= k\cos(\theta)\sin(\phi) \\ K_y &= k\sin(\theta)\sin(\phi) \\ K_z &= k\cos(\phi) \end{aligned} \tag{A.8}$$

and noting $A = \frac{v_{at}\Delta\varepsilon^2}{(2\pi)^3}\left(\frac{1+\nu}{1-\nu}\right)^2$, we have from Eq. (15):

$$\begin{aligned} U_{zz}(d\boldsymbol{e_z}) &= A\int_{-\infty}^{+\infty}\int_{-\infty}^{+\infty}\int_{-\infty}^{+\infty}\frac{K_z^2}{\boldsymbol{K}^2}\cos(K_z d)\exp(-a^2\boldsymbol{K}^2)dK_x dK_y dK_z \\ &= A\int_0^{2\pi}d\theta\int_0^{\pi}d\phi\sin(\phi)\int_0^{\infty}dk\cos^2(\phi)\cos(kd\cos(\phi))\exp(-a^2k^2) \\ &= 4\pi A\int_0^{\pi/2}d\phi\sin(\phi)\cos^2(\phi)\int_0^{\infty}dk\cos(kd\cos(\phi))\exp(-a^2k^2). \end{aligned} \tag{A.9}$$

Using the expression of I_0 in Eq. (A.1), we have

$$U_{zz}(d\boldsymbol{e_z}) = \frac{2\pi^{3/2}A}{a}\int_0^{\pi/2}d\phi\sin(\phi)\cos^2(\phi)\exp\left(-\frac{d^2\cos^2(\phi)}{4a^2}\right). \tag{A.10}$$

Introducing the variable $u = d\cos(\phi)/2a$ yields:

$$U_{zz}(d\boldsymbol{e_z}) = \frac{2\pi^{3/2}A}{a}\left(\frac{2a}{d}\right)^3\int_0^{d/2a}du\ u^2\exp(-u^2). \tag{A.11}$$

Using Eq. (A.5), we obtain

$$U_L(d) = U_{zz}(d\boldsymbol{e_z}) = \frac{8A\pi^{3/2}}{a}\left(\frac{a}{d}\right)^3\left[\frac{\sqrt{\pi}}{2}\mathrm{erf}\left(\frac{d}{2a}\right) - \frac{d}{2a}\exp\left(-\frac{d^2}{4a^2}\right)\right] \tag{A.12}$$

Finally, using the expression of the mean-square displacement $\langle u^2 \rangle$ given in Ref. [17], we find

$$U_L(d) = 4\langle u^2 \rangle \left(\frac{a}{d}\right)^3 \left[\frac{\sqrt{\pi}}{2}\mathrm{erf}\left(\frac{d}{2a}\right) - \frac{d}{2a}\exp\left(-\frac{d^2}{4a^2}\right)\right], \tag{A.13}$$

Appendix A.3. Computation of $\Sigma_T(d)$

The stress correlations are derived similarly to the displacement correlations using polar coordinates. We only detail one example here. Starting from Eq. (25), we have

$$\begin{aligned}\Sigma_{xy,xy}(d\boldsymbol{e_z}) &= 4\mu^2 A \int_{-\infty}^{+\infty}\int_{-\infty}^{+\infty}\int_{-\infty}^{+\infty} \frac{K_x^2 K_y^2}{\boldsymbol{K}^4}\cos(K_z d)e^{-a^2\boldsymbol{K}^2} dK_x dK_y dK_z \\ &= 4\mu^2 A \int_0^{2\pi} d\theta \int_0^{\pi} d\phi \sin(\phi) \int_0^{\infty} dk k^2 \cos^2(\theta)\sin^2(\theta)\sin^4(\phi)\cos(kd\cos(\phi))e^{-a^2k^2} \\ &= 2\mu^2 A\pi \int_0^{\pi/2} d\phi \sin^5(\phi) \int_0^{\infty} dk\ k^2 \cos(kd\cos(\phi))e^{-a^2k^2}. \end{aligned} \tag{A.14}$$

Using the expression of I_2 in Eq. (A.2), we have

$$\Sigma_{xy,xy}(d\boldsymbol{e_z}) = \frac{\mu^2 A\pi^{3/2}}{2a^3}\int_0^{\pi/2} d\phi \sin^5(\phi)\left(1 - \frac{d^2\cos^2(\phi)}{2a^2}\right)e^{-\frac{d^2\cos^2(\phi)}{4a^2}}. \tag{A.15}$$

Introducing the variable $u = d\cos(\phi)/2a$,

$$\Sigma_{xy,xy}(d\boldsymbol{e_z}) = \mu^2 A\frac{\pi^{3/2}}{a^3}\left(\frac{a}{d}\right)\int_0^{d/2a} du \left(1 - \frac{4a^2}{d^2}u^2\right)^2 \left(1 - 2u^2\right)e^{-u^2}. \tag{A.16}$$

Using Eqs. (A.4-A.7), we obtain

$$\Sigma_T(d) = \Sigma_{xy,xy}(d\boldsymbol{e_z}) = \frac{4\mu^2 A\pi^{3/2}}{a^3}\left(\frac{a}{d}\right)^3\left[\sqrt{\pi}\left(1 - \frac{6a^2}{d^2}\right)\mathrm{erf}\left(\frac{d}{2a}\right) + \frac{6a}{d}e^{-d^2/4a^2}\right]. \tag{A.17}$$

Finally, using the expression of the mean-square stress $\langle \tau^2 \rangle$ given in Ref. [17], we have

$$\Sigma_T(d) = 15\langle \tau^2 \rangle \left(\frac{a}{d}\right)^3\left[\sqrt{\pi}\left(1 - \frac{6a^2}{d^2}\right)\mathrm{erf}\left(\frac{d}{2a}\right) + \frac{6a}{d}\exp\left(-\frac{d^2}{4a^2}\right)\right]. \tag{A.18}$$

References

[1] R.L. Fleischer. Substitutional solution hardening. Acta Metall., 11(3):203–209, 1963.

[2] R. Labusch. A statistical theory of solid solution hardening. Phys. Stat. Sol. (b), 41(2):659–669, 1970.

[3] H. Suzuki. Solution hardening in Au-Ag and Cu-Ni alloy crystals. Proceedings of the 8th International Conference on the Strength of Metals and Alloys, 2:573–578, 1989.

[4] J.-W. Yeh. Recent progress in high entropy alloys. Ann. Chim. Sci. Mat, 31(6):633–648, 2006.

[5] Y. Zhang, T.T. Zuo, Z. Tang, M.C. Gao, K.A. Dahmen, P.K. Liaw, and Z.P. Lu. Microstructures and properties of high-entropy alloys. Prog. Mater. Sci., 61:1–93, 2014.

[6] O.N. Senkov, D.B. Miracle, K.J. Chaput, and J.-P. Couzinié. Development and exploration of refractory high entropy alloys - A review. J. Mater. Res., 33(19):3092–3128, 2018.

[7] J.-W. Yeh, S.-Y. Chang, Y.-D. Hong, S.-K. Chen, and S.-J. Lin. Anomalous decrease in X-ray diffraction intensities of Cu–Ni–Al–Co–Cr–Fe–Si alloy systems with multi-principal elements. Mater. Chem. Phys., 103(1):41–46, 2007.

[8] Y. Zou, S. Maiti, W. Steurer, and R. Spolenak. Size-dependent plasticity in an $Nb_{25}Mo_{25}Ta_{25}W_{25}$ refractory high-entropy alloy. Acta Mater., 65:85–97, 2014.

[9] H.S. Oh, D. Ma, G.P. Leyson, B. Grabowski, E.S. Park, F. Körmann, and D. Raabe. Lattice distortions in the FeCoNiCrMn high entropy alloy studied by theory and experiment. Entropy, 18(9):321, 2016.

[10] Y. Tong, K. Jin, H. Bei, J.Y.P. Ko, D.C. Pagan, Y. Zhang, and F.X. Zhang. Local lattice distortion in NiCoCr, FeCoNiCr and FeCoNiCrMn concentrated alloys investigated by synchrotron X-ray diffraction. Mater. and Design, 155:1–7, 2018.

[11] L.R. Owen, E.J. Pickering, H.Y. Playford, H.J. Stone, M.G. Tucker, and N.G. Jones. An assessment of the lattice strain in the CrMnFeCoNi high-entropy alloy. Acta Mater., 122:11–18, 2017.

[12] L.R. Owen and N.G. Jones. Lattice distortions in high-entropy alloys. J. Mater. Res., 33(19):2954–2969, 2018.

[13] N.L. Okamoto, K. Yuge, K. Tanaka, H. Inui, and E.P. George. Atomic displacement in the CrMnFeCoNi high-entropy alloy–a scaling factor to predict solid solution strengthening. AIP Advances, 6(12):125008, 2016.

[14] Y.F. Ye, Y.H. Zhang, Q.F. He, Y. Zhuang, S. Wang, S.Q. Shi, A. Hu, J. Fan, and Y. Yang. Atomic-scale distorted lattice in chemically disordered equimolar complex alloys. Acta Mater., 150:182–194, 2018.

[15] H. Song, F. Tian, Q.-M. Hu, L. Vitos, Y. Wang, J. Shen, and N. Chen. Local lattice distortion in high-entropy alloys. Phys. Rev. Mater., 1(2):023404, 2017.

[16] B. Feng and M. Widom. Elastic stability and lattice distortion of refractory high entropy alloys. Mater. Chem. Phys., 210:309–314, 2018.

[17] P.-A. Geslin and D. Rodney. Microelasticity model of random alloys. Part I: mean square displacements and stresses. submitted to J. Mech. Phys. Solids, 2020.

[18] W.G. Nöhring and W.A. Curtin. Correlation of microdistortions with misfit volumes in high entropy alloys. Scripta Mater., 168:119–123, 2019.

[19] A.G. Khachaturyan. Theory of structural transformations in solids. John Wiley and Sons Inc., 1983.

[20] T. Mura. Micromechanics of defects in solids. Martinus Nijhoff, 1987.

[21] K. Huang. X-ray reflexions from dilute solid solutions. Proc. R. Soc. Lond. Ser A, 190(1020):102–117, 1947.

[22] R.I. Barabash, J.S. Chung, and M.F. Thorpe. Lattice and continuum theories of huang scattering. J. Phys. Cond. Mat., 11(15):3075, 1999.

[23] M.F. Thorpe, J.S. Chung, and Y. Cai. Diffraction from random alloys. Phys. Rev. B, 43(10):8282, 1991.

[24] F. Glas. Correlated static atomic displacements and transmission-electron-microscopy contrast in compositionally homogeneous disordered alloys. Phys. Rev. B, 51(2):825, 1995.

[25] A.-L. Barabási and H.E. Stanley. Fractal concepts in surface growth. Cambridge University Press, 1995.

[26] S. Zapperi and M. Zaiser. Depinning of a dislocation: the influence of long-range interactions. Mater. Sci. Eng. A, 309:348–351, 2001.

[27] E. Medina, T. Hwa, M. Kardar, and Y.-C. Zhang. Burgers equation with correlated noise: Renormalization-group analysis and applications to directed polymers and interface growth. Phys. Rev. A, 39(6):3053, 1989.

[28] K. Park and I.-M. Kim. Dynamics of an interface driven through random media: The effect of a spatially correlated noise. J. Phys. Soc. Jap., 72(1):111–116, 2003.

[29] A. Lemaître. Structural relaxation is a scale-free process. Phys. Rev. Lett., 113(24):245702, 2014.

[30] A. Lemaître. Tensorial analysis of Eshelby stresses in 3D supercooled liquids. J. Chem. Phys., 143(16):164515, 2015.

[31] A. Lemaître. Stress correlations in glasses. J. Chem. Phys., 149(10):104107, 2018.

[32] G.P.M. Leyson, W.A. Curtin, L.G. Hector, and C.F. Woodward. Quantitative prediction of solute strengthening in aluminium alloys. Nat. Mater., 9(9):750–755, 2010.

[33] C. Varvenne, A. Luque, and W.A. Curtin. Theory of strengthening in FCC high entropy alloys. Acta Mater., 118:164–176, 2016.

[34] I. Toda-Caraballo and P.E.J. Rivera-Díaz-del Castillo. Modelling solid solution hardening in high entropy alloys. Acta Mater., 85:14–23, 2015.

[35] J.-H. Zhai and M. Zaiser. Properties of dislocation lines in crystals with strong atomic-scale disorder. Mater. Sci. Eng. A, 740:285–294, 2019.

[36] B. Yin, S. Yoshida, N. Tsuji, and W.A. Curtin. Yield strength and misfit volumes of NiCoCr and implications for short-range-order. Nat. Comm., 11(1):2507, 2020.

[37] E. Antillon, C. Woodward, S.I. Rao, B. Akdim, and T.A. Parthasarathy. Chemical short range order strengthening in a model FCC high entropy alloy. Acta Mater., 2020.

[38] C. Varvenne, A. Luque, W.G. Nöhring, and W.A. Curtin. Average-atom interatomic potential for random alloys. Phys. Rev. B, 93(10):104201, 2016.

[39] S. Plimpton. Fast parallel algorithms for short-range molecular dynamics (http://lammps.sandia.gov). J. Comp. Phys., 117(1):1–19, 1995.

[40] R.O. Scattergood and D.J. Bacon. The Orowan mechanism in anisotropic crystals. Phil. Mag., 31(1):179–198, 1975.

[41] R.O. Scattergood and D.J. Bacon. The strengthening effect of voids. Acta Metall., 30(8):1665–1677, 1982.

[42] R.M. Elder, W.D. Mattson, and T.W. Sirk. Origins of error in the localized virial stress. Chem. Phys. Lett., 731:136580, 2019.

[43] P.S. Branicio and D.J. Srolovitz. Local stress calculation in simulations of multicomponent systems. J. Comp. Phys., 228(22):8467–8479, 2009.

[44] N.C. Admal and E.B. Tadmor. A unified interpretation of stress in molecular systems. J. Elasticity, 100(1-2):63–143, 2010.

[45] X.-Y. Liu and J.B. Adams. Grain-boundary segregation in Al–10%Mg alloys at hot working temperatures. Acta Mater., 46(10):3467–3476, 1998.

[46] C. Varvenne, F. Bruneval, M.-C. Marinica, and E. Clouet. Point defect modeling in materials: Coupling ab initio and elasticity approaches. Phys. Rev. B, 88(13):134102, 2013.

[47] B. Borie and C.J. Sparks. The interpretation of intensity distributions from disordered binary alloys. Acta Crystallogr. Sec. A, 27(3):198–201, 1971.

[48] C.G. Shirley. Correlations and interactions in disordered binary alloys with atomic-radius disparity. Phys. Rev. B, 10(4):1149, 1974.

[49] B. Borie and C.J. Sparks. The short-range structure of copper–16 at.% aluminum. Acta Crystallogr., 17(7):827–835, 1964.

[50] P. Singh, A.V. Smirnov, and D.D. Johnson. Atomic short-range order and incipient long-range order in high-entropy alloys. Phys. Rev. B, 91(22):224204, 2015.

[51] P.-A. Geslin and D. Rodney. Thermal fluctuations of dislocations reveal the interplay between their core energy and long-range elasticity. Phys. Rev. B, 98(17):174115, 2018.

[52] P.-A. Geslin and D. Rodney. Investigation of partial dislocations fluctuations yields dislocation core parameters. Model. Sim. Mater. Sci. Eng., 28(5):055006, 2020.

[53] G. Péterffy, P.D. Ispánovity, M.E. Foster, X. Zhou, and R.B. Sills. Length scales and scale-free dynamics of dislocations in dense solid solutions. Materials Theory, 4(1):1–25, 2020.

[54] Y. Zeng, X. Cai, and M. Koslowski. Effects of the stacking fault energy fluctuations on the strengthening of alloys. Acta Mater., 164:1–11, 2019.

[55] C. Sobie, L. Capolungo, D.L. McDowell, and E. Martinez. Scale transition using dislocation dynamics and the nudged elastic band method. J. Mech. Phys. Sol., 105:161–178, 2017.

[56] P.-A. Geslin, R. Gatti, B. Devincre, and D. Rodney. Implementation of the nudged elastic band method in a dislocation dynamics formalism: application to dislocation nucleation. J. Mech. Phys. Sol., 108:49–67, 2017.

[57] A. Arsenlis, W. Cai, M. Tang, M. Rhee, T. Oppelstrup, G. Hommes, T.G. Pierce, and V.V. Bulatov. Enabling strain hardening simulations with dislocation dynamics. Model. Sim. Mater. Sci. Eng., 15(6):553, 2007.

[58] B. Devincre, R. Madec, G. Monnet, S. Queyreau, R. Gatti, and L. Kubin. Modeling crystal plasticity with dislocation dynamics simulations: the microMegas code. In Mechanics of nano-objects, pages 81–100. Presses des Mines, 2011.

[59] Y. Sato, T. Swinburne, S. Ogata, and D. Rodney. Anharmonic effect on the thermally-activated migration of $10\bar{1}2$ twin interfaces in magnesium. Mat. Res. Lett., 9(5):231–238, 2021.